



A Method to Combine Residual Stress Measurements from XRD and IHD using Series Expansion

T. C. Smit¹ · R. G. Reid¹

Received: 27 July 2020 / Accepted: 5 April 2021 / Published online: 17 April 2021
© Society for Experimental Mechanics 2021

Abstract

Background It is common practice to use various residual stress measurement methods to complement each other and fully define a through-thickness stress distribution. Incremental hole-drilling (IHD) and X-ray diffraction (XRD) are two of the most widely used techniques. Although IHD readily provides stress data to some depth, the method is susceptible to large stress uncertainties near the surface. XRD, in contrast, is most suited to finding near-surface stresses.

Objective Constrain the residual stress distributions obtained through series expansion by using XRD measurements, thereby obtaining full depth stress measurements with reduced uncertainty near the surface.

Method The proposed method enforces suitable relationships between the amplitude coefficients of the series expansion such that the resultant stress distributions match the XRD measurements. The method is demonstrated on an aluminium alloy 7075 specimen of 10 mm thickness that underwent laser shock peening treatment.

Results Strong correlation in calculated residual stress distributions was found between the proposed method, standard series expansion and the regularized integral method. The proposed method has reduced stress uncertainty near the surface when compared to both standard series expansion and integral methods of IHD due to its incorporation of near-surface XRD data.

Conclusions The proposed method allows XRD measurements to be rigorously incorporated into IHD results. The effect of XRD uncertainty on the overall IHD stress distribution is localised to the near-surface measurements.

Keywords Residual stress · Incremental hole-drilling · Series expansion · X-ray diffraction

Introduction

Laser Shock Peening (LSP) is a surface treatment technique that uses pulsed, high intensity, laser irradiation to generate beneficial residual compressive stress at and near the surface. This can improve resistance to fatigue [1] and crack initiation and propagation [2]. The residual stress distribution induced by LSP can be challenging to measure accurately since it usually exhibits steep variations near the surface and a local minimum within the first 0.4 mm from the surface. The magnitude and distribution of the LSP-induced compressive stress depends on the combined effects of the laser specification and numerous LSP parameters. It is, therefore, important to be able to accurately measure the result-

ing residual stress distribution so that the effects of these parameters can be determined. X-ray diffraction (XRD) and incremental hole-drilling (IHD) are two of the most commonly used methods to measure these residual stresses [3].

XRD is a non-destructive, near-surface measurement technique that can be used to determine the residual stress from the strain and associated X-ray elastic constants in a crystal lattice [4]. XRD measurements are made with the plane stress assumption where the stress normal to the surface is zero [5]. High energy X-rays, which penetrate a small distance below the surface, are used to irradiate a specimen. Crystal lattice planes diffract the X-rays according to Bragg's Law and detectors record the intensity of the diffracted rays at different angular positions as they rotate around the specimen. A widely used method is the $\sin^2 \psi$ approach [6] where the lattice spacing is measured for a range of ψ tilts. Lattice spacing is plotted against $\sin^2 \psi$ and the stress is determined from the slope of a linear or elliptical least-squares fit to the data. Large grain sizes can adversely affect the XRD measurement since

✉ R. G. Reid
robert.reid@wits.ac.za

¹ School of Mechanical, Industrial and Aeronautical Engineering, University of the Witwatersrand, Private Bag 3, Wits 250, South Africa



fewer grains within the irradiated volume contribute to the diffraction peak. This results in lower peak intensities and reduced accuracy in location of the peaks [5]. The texture of the material is also important since it can cause large variation in diffraction peak intensity between ψ tilts. This effect can be mitigated somewhat by using appropriate ψ tilts and by oscillation in ψ by typically $\pm 2^\circ$ such that grains over a larger area contribute to the measurement [5]. Since X-rays penetrate some depth into the specimen, the measured strain and residual stress is essentially an average over the penetration depth of a few microns below the surface, up to 20–30 μm for aluminium alloys [7]. The surface roughness of the sample should clearly, therefore, be smaller than the penetration depth [8]. The penetration depth depends on various parameters such as the linear absorption coefficient of the material, ψ tilt, diffraction peak intensities and Bragg reflection angle [4]. If measurement of a residual stress profile beneath the surface layer is required, successive XRD measurements with removal of layers between measurements is necessary [3, 5].

Residual stress measurements from XRD can be prone to relatively high uncertainty since the technique is sensitive to small variations in the crystal lattice [4, 9] and to errors arising from the possible difficulty in determining the position of the diffraction peak [5], operator skill, uncertainty in alignment and equipment calibration. Therefore, a robust experimental technique is required to minimise the effect of various measurement uncertainty sources [10]. A thorough uncertainty estimation for XRD is difficult since many uncertainty sources are non-quantifiable [5]. The main XRD uncertainty sources have been investigated by inter-laboratory comparisons [11] with 16 participating laboratories using 21 different XRD instruments. The largest sources of measurement uncertainty were found to be associated with the peak fitting software and the operator. Total measurement uncertainty in the region of ± 20 MPa is common [9, 12].

IHD is a semi-destructive residual stress measurement technique and has an ASTM Standard Test Procedure, ASTM E837-13a [13]. The method of determining the through-thickness variation of all three in-plane stress components is based on the assumptions that the stress component normal to the surface is negligible, and that no significant residual stress is induced by the IHD process. Stressed material is removed from the hole being drilled, with the consequent release of strain which is typically measured using a strain gauge rosette. Since the strain measurements are taken some distance from the location where stressed material is removed and because the strain field around the hole is not uniform, an inverse solution is required to calculate the residual stress distribution from the incremental strain measurements. The inverse solution makes use of ‘calibration coefficients’ that can be determined using

finite element (FE) calculations for known through-thickness stress distributions [14]. The integral method is the most widely used computational method for IHD and is used in the ASTM standard. It assumes that unit pulses of uniform stress exist at each incremental hole depth when determining the calibration coefficients [13, 15]. This assumption does not have a substantial detrimental effect when making many small depth increments and identifying the stress depth at the mid-step depth, especially when combined with Tikhonov regularization [16]. Tikhonov regularization is usually employed to remove noise artefacts from the residual stress distribution by allowing a misfit between the measured strain data and that used in the inverse solution. The extent of regularization must be carefully considered, however, as it can distort the calculated stresses [13].

Significant work has been done to extend the use of the integral method with IHD to nearly all applications and to correct common errors such as hole bottom fillet radius [17], hole offset [18–20], plasticity effects [21, 22] etc. Experimental and analytical studies have been conducted [23] which have found that errors arising from localised yielding around the hole are negligible if the residual stress is below 70% of the yield strength of the specimen material. However, when the residual stress exceeds this limit, errors of 10% to 30% have been reported [23]. This limit may be insufficient for stress distributions with high gradients [21] and a limit of 60% of the yield strength is more appropriate [24]. IHD with the integral method has been successfully used to measure residual stresses induced by shot peening [25] and LSP [26] in aluminium with good correlation to XRD measurements. Small depth increments can be used with Tikhonov regularization to capture the LSP-induced residual stress profile which varies steeply beneath the surface. The continuity characteristics of the regularized integral solution also allow the interior data to be extrapolated to the surface and, with modern fine-increment drilling, the distance to be extrapolated is small.

Series expansion [14] is an alternative to the integral method, where it is assumed that the residual stress distribution can be expanded into stress distributions defined by power series. The inverse solution makes use of least-squares curve fitting and the method is therefore more tolerant of measurement noise. It is beneficial to the least-squares solution to have many more strain measurements, through the use of small depth increments, than coefficients of series orders that need to be determined by the inverse solution [27]. A recent investigation using eigenstrain [28] has shown that series expansion remains stable at higher orders and can reduce the overall stress uncertainty, provided that a sufficient number of depth increments are used and convergence of the solution is found by comparing the stress distributions and associated uncertainties of a number of series orders. While series expansion can directly provide an estimate of the residual stress at or near the



surface, the extrapolated stress distributions are susceptible to high uncertainty near the surface due to the series being less constrained at their ends. Additionally, since the first hole drilling increment accumulates the effects of the stresses within that depth, both integral method and series expansion results are effectively slightly removed from the exact surface.

While XRD can be used to determine the important surface stresses, measurement of the residual stress distribution beneath the surface requires successive layer removal and XRD measurements on each new surface. This reduces the utility of the method in this situation. In contrast, a physical characteristic of the IHD method is that it is susceptible to large stress uncertainties near the surface, independent of the stress computation method used. This is primarily due to uncertainty in establishing the the zero depth datum of the measured strain data which similarly affects both series expansion and integral methods. To overcome this limitation of IHD, a method of incorporating near-surface XRD measurements into a set of IHD measurements is proposed in this work. While the integral method is easier and more practical to use in most situations, incorporating near-surface XRD measurements is more easily achievable using series expansion than the conventional approach because series expansion makes use of mathematical functions to describe the stress distribution throughout the depth. This facilitates the constraint of the series to match the XRD data in a mathematically rigorous way. The method is demonstrated on an aluminium alloy 7075 plate of 10 mm thickness with a rapidly varying through-thickness stress distribution induced by LSP. Power series expansion of eigenstrain is generated through the use of temperature variations to obtain calibration coefficients using FE calculations. Constrained least-squares error minimisation is employed in the inverse solution to determine the amplitudes of each term in the eigenstrain series that results in a best fit to the measured data, while satisfying the near-surface stress conditions of the XRD measurements. These amplitudes are used with the far-field stress distributions generated by each contributing eigenstrain series to completely define the residual stress distribution. Uncertainties are estimated through the use of Monte Carlo simulation.

Existing IHD Computational Methods

Integral Method

The integral method is well known and fully documented in the ASTM Standard Test Procedure, ASTM E837-13a [13], and is therefore only briefly described here. Calibration matrices, \bar{a} and \bar{b} , are used to calculate the residual stresses from the released strains. The \bar{a} and \bar{b} matrices can be determined by FE calculations for the release of unit equi-biaxial

and shear stress at each incremental depth, respectively. The ASTM standard provides calibration tables for 20 depth increments and suggests the use of Tikhonov regularization [16] to remove noise artefacts from the calculated stress distributions. Tikhonov regularization is employed by using the tri-diagonal ‘second derivative’ matrix, c , in the form:

$$[c] = \begin{bmatrix} 0 & 0 & & & & \\ -1 & 2 & -1 & & & \\ & -1 & 2 & -1 & & \\ & & -1 & 2 & -1 & \\ & & & 0 & 0 & \end{bmatrix} \quad (1)$$

where the number of rows is equal to the number of depth increments used.

Equations (2)-(4) are used to calculate the residual distributions.

$$([\bar{a}]^T [\bar{a}] + \alpha_P [c]^T [c]) \{P\} = \frac{E}{1 + \nu} [\bar{a}]^T \{p\} \quad (2)$$

$$([\bar{b}]^T [\bar{b}] + \alpha_Q [c]^T [c]) \{Q\} = E [\bar{b}]^T \{q\} \quad (3)$$

$$([\bar{b}]^T [\bar{b}] + \alpha_T [c]^T [c]) \{T\} = E [\bar{b}]^T \{t\} \quad (4)$$

where P is the vector of through-thickness isotropic (equi-biaxial) stresses, Q is the 45° shear stresses, T is the x - y shear stresses and p , q and t are combination strain vectors [13]. The Cartesian stresses at each depth increment can be found from P , Q and T [13].

The extent of regularization can be varied using the factors α_P , α_Q and α_T . Zero values for these factors apply zero regularization and increasing values progressively smooth the stress results. The amount of regularization that is applied can be optimised iteratively using the Morozov Discrepancy Principle [16]. Insufficient regularization leads to noise artefacts in the calculated stresses, while excessive regularization can distort the stress results. A misfit exists between the regularized strains that correspond to the calculated stresses (P , Q and T) using Equations (2)-(4) and the experimental combination strains p , q and t .

Series Expansion

The FE method is used to generate known far-field stress distributions, S , resulting from applied eigenstrains which vary in the through-thickness direction according to power series in each of the three in-plane strain components. The calibration matrix, C , is determined from the strain response at each strain gauge location as the depth of the hole is increased for each applied eigenstrain [28]. The experimental strain vector, ϵ_{meas} , is used with the calibration matrix in



a least-squares inverse solution to determine the amplitude vector, A :

$$\{A\} = ([C]^T[C])^{-1}[C]^T\{\epsilon_{meas}\} \tag{5}$$

where A contains the amplitudes of the applied eigenstrain functions that best match the experimental strain response.

The calculated amplitude vector is used to determine the residual stress distribution vector, σ_{res} , for the specimen using Equation (6) [28]:

$$\{\sigma_{res}\} = [S]\{A\} \tag{6}$$

Constrained Series Expansion

The method proposed in this work is to constrain the near-surface stress solution, $\sigma_{surface}$, of the series expansion method to the measurements obtained from XRD:

$$\begin{aligned} \{\sigma_{surface}\} &= \{\sigma_{XRD}\} \\ \text{or} & \\ [Q]\{A\} &= \{\sigma_{XRD}\} \end{aligned} \tag{7}$$

where matrix Q comprises three rows representing each of the stress components and which is extracted from the stress matrix, S , at the depth of the XRD measurements.

$$[Q] = [S_{surface}] = \begin{bmatrix} S_{1_{xx0}} & \dots & S_{1_{xy0}} & \dots & S_{1_{xxj_0}} & \dots & S_{1_{xyj_n}} \\ S_{1_{yy0}} & \dots & S_{1_{yy0}} & \dots & S_{1_{yyj_0}} & \dots & S_{1_{yyj_n}} \\ S_{1_{xy0}} & \dots & S_{1_{xy0}} & \dots & S_{1_{xyj_0}} & \dots & S_{1_{xyj_n}} \end{bmatrix} \tag{8}$$

where j is the component of eigenstrain, and n is the order of the applied eigenstrain.

The imposition of constraints onto the series solution means that the amplitude coefficients, A , are not all independent. It is necessary, therefore, to split these terms into independent and dependent terms. Matrices A and Q are therefore decomposed into \hat{A} and \bar{A} , and Q_A and Q_B , respectively:

$$\{A\} = \begin{Bmatrix} \hat{A} \\ \bar{A} \end{Bmatrix}, \quad [Q] = [Q_A \quad Q_B] \tag{9}$$

where \hat{A} represents the vector of independent amplitude coefficients, \bar{A} represents the vector of dependent amplitude coefficients, and Q_B is a square invertible matrix. Equation (7) can now be rewritten as:

$$\begin{aligned} [Q_A]\{\hat{A}\} + [Q_B]\{\bar{A}\} &= \{\sigma_{XRD}\} \\ [Q_B]\{\bar{A}\} &= -[Q_A]\{\hat{A}\} + \{\sigma_{XRD}\} \\ \{\bar{A}\} &= -[Q_B]^{-1}[Q_A]\{\hat{A}\} + [Q_B]^{-1}\{\sigma_{XRD}\} \end{aligned} \tag{10}$$

Therefore:

$$\begin{aligned} \{A\} &= \begin{bmatrix} I \\ -[Q_B]^{-1}[Q_A] \end{bmatrix} \{\hat{A}\} + \begin{Bmatrix} 0 \\ [Q_B]^{-1}\{\sigma_{XRD}\} \end{Bmatrix} \\ &= [G]\{\hat{A}\} + \{H\} \end{aligned} \tag{11}$$

The experimental strain vector, ϵ_{meas} , is used with the matrix of calibration coefficients in a constrained least-squares inverse solution to determine the vector of independent amplitude coefficients, \hat{A} . In vector-matrix form:

$$\begin{aligned} \{\epsilon_{meas}\} &= [C]\{A\} \\ \{\epsilon_{meas}\} &= [C]([G]\{\hat{A}\} + \{H\}) \\ [G]^T[C]^T\{\{\epsilon_{meas}\} - [C]\{H\}\} &= [G]^T[C]^T[C][G]\{\hat{A}\} \\ \{\hat{A}\} &= ([G]^T[C]^T[C][G])^{-1}[G]^T[C]^T\{\{\epsilon_{meas}\} - [C]\{H\}\} \end{aligned} \tag{12}$$

Finally, the amplitude vector, A , containing the amplitudes of the applied eigenstrain distributions which best match the experimental strain response, while ensuring that stress magnitude near the surface is constrained to the results obtained using XRD can be found using Equation (11). The calculated amplitude vector is used with the stress matrix, S , to determine the residual stress distributions using Equation (6). The use of a least-squares approach reduces sensitivity to strain measurement errors and subsequent uncertainty in calculated stress. To achieve a robust least-squares fit, the number of terms in ϵ_{meas} must be significantly greater than in \hat{A} . Therefore, it is beneficial to use small experimental depth increments to obtain a large strain data set. The most appropriate series order can be determined from the size and convergence of the associated uncertainties in the residual stress distributions [29].

Practical Example

Specimen and LSP

A rolled aluminium alloy 7075-T651 plate was reduced from 15 mm thickness to 10 mm by machining 1 mm from the top face of the plate and 4 mm from the bottom before preparing individual specimens of 60 mm × 60 mm. The mechanical



Table 1 Mechanical properties and chemical composition of aluminium alloy 7075-T651 [30]

Young's Modulus (MPa)	Poisson's ratio	Tensile Yield Strength (MPa)	Chemical composition Wt. (%)									
			Al ¹	Cr ¹	Cu ¹	Fe ²	Mg ¹	Mn ²	Si ²	Ti ²	Zn ¹	
71700	0.33	503	89.3	0.23	1.6	0.5	2.5	0.3	0.4	0.2	5.6	

¹Average value

²Maximum value

properties and the chemical composition of aluminium alloy 7075-T651 are shown in Table 1.

LSP treatment was applied to the upper face of the specimen at the National Laser Centre (NLC) of the Council for Scientific and Industrial Research (CSIR) in Pretoria, South Africa, using a Quanta-Ray Pro Spectra Physics (QRPSP) Nd:YAG laser. The specifications of the laser and the parameters used during LSP are shown in Table 2. A 1.5 mm spot diameter, with a spot density of 5 spots/mm² (70% spot overlap), was used to attain a power intensity of 1.5 GW/cm² with an equidistant raster pattern as the spot sequence strategy. LSP was applied to an area of 11.25 mm × 11.25 mm. In this work the LSP step and scan directions are represented by the *x* and *y* directions, respectively.

XRD

Laboratory XRD was used to obtain the near-surface residual stresses to constrain the IHD measurements. The sin² ψ method [6] was performed using a Proto iXRD (Proto Manufacturing Inc., Taylor, Michigan USA) instrument at the CSIR. Lattice spacing of the {311} planes was measured for 7 angles between -27° and +27° using Cr-K α radiation with a wavelength of 2.291 Å at a Bragg angle of approximately 139°. Measurements were taken using a 2 mm round aperture at 0°, 45°, and 90° with respect to the LSP raster pattern to obtain the in-plane stress-tensor. At each tilt angle, the sample was oscillated by $\pm 3^\circ$ in ψ to improve counting statistics and reduce the effect of large grain sizes and texture in the aluminium specimen. The residual stresses were calculated for plane stress conditions using X-ray elastic constants of $\frac{1}{2}S_2 = 19.54 \times 10^{-6} \text{ MPa}^{-1}$ and $S_1 = -5.11 \times 10^{-6} \text{ MPa}^{-1}$ for the {311} lattice plane. The XRD information depth was estimated to be 10.5 μm [31].

IHD

The Sint Technology Restan MTS 3000 incremental hole-drilling machine, with a high-speed pneumatic turbine, was used to conduct IHD. A tungsten carbide inverted cone end mill with a diameter of 1.6 mm was used to cut the hole in the centre of the LSP area. The hole diameter was measured after IHD as 1.78 mm using the built-in microscope and micrometers of the Restan MTS 3000. Drilling ceased at a depth of 1.2 mm since the region of high compressive stress resulting from LSP lies close to the surface and the sensitivity of the surface strain measurements greatly decreases beyond a depth of approximately half the hole diameter.

Six element rectangular HBM foil strain gauge rosettes of type 1.5/350M RY61 were used for the IHD experiment. The use of a six element rosette somewhat mitigates the effect of drilling offset errors. Temperature compensation was employed by connecting each active gauge of the 1.5/350M RY61 rosette to the corresponding gauge of a dummy 1.5/350M RY61 rosette, attached to the same specimen type, in a quarter bridge configuration using a National Instruments data acquisition system equipped with a SCXI-1520 strain gauge card. The experimentally measured strain variations at the *x*, *y* and 45° strain gauge locations are presented in Fig. 1.

Computational

The 1.5/350M RY61 strain gauge rosette used in this work has a different geometry to those specified in the ASTM standard and the hole diameter of 1.78 mm lies outside the suggested range of 1.88 - 2.12 mm [13]. The calibration coefficients must, therefore, be determined using FE analysis since the ASTM calibration coefficients are not applica-

Table 2 Laser specifications and LSP parameters

QRPSP Laser Specifications						LSP Parameters		
Laser Type	Wavelength (nm)	Pulse Frequency (Hz)	Energy Range (J)	Spot Shape	Spot Size Range (mm)	Power Intensity (GW/cm ²)	Spot Diameter (mm)	Coverage (spots/mm ²)
Nd:YAG	1064	20	0.2-1	o	0.5-2.5	1.5	1.5	5



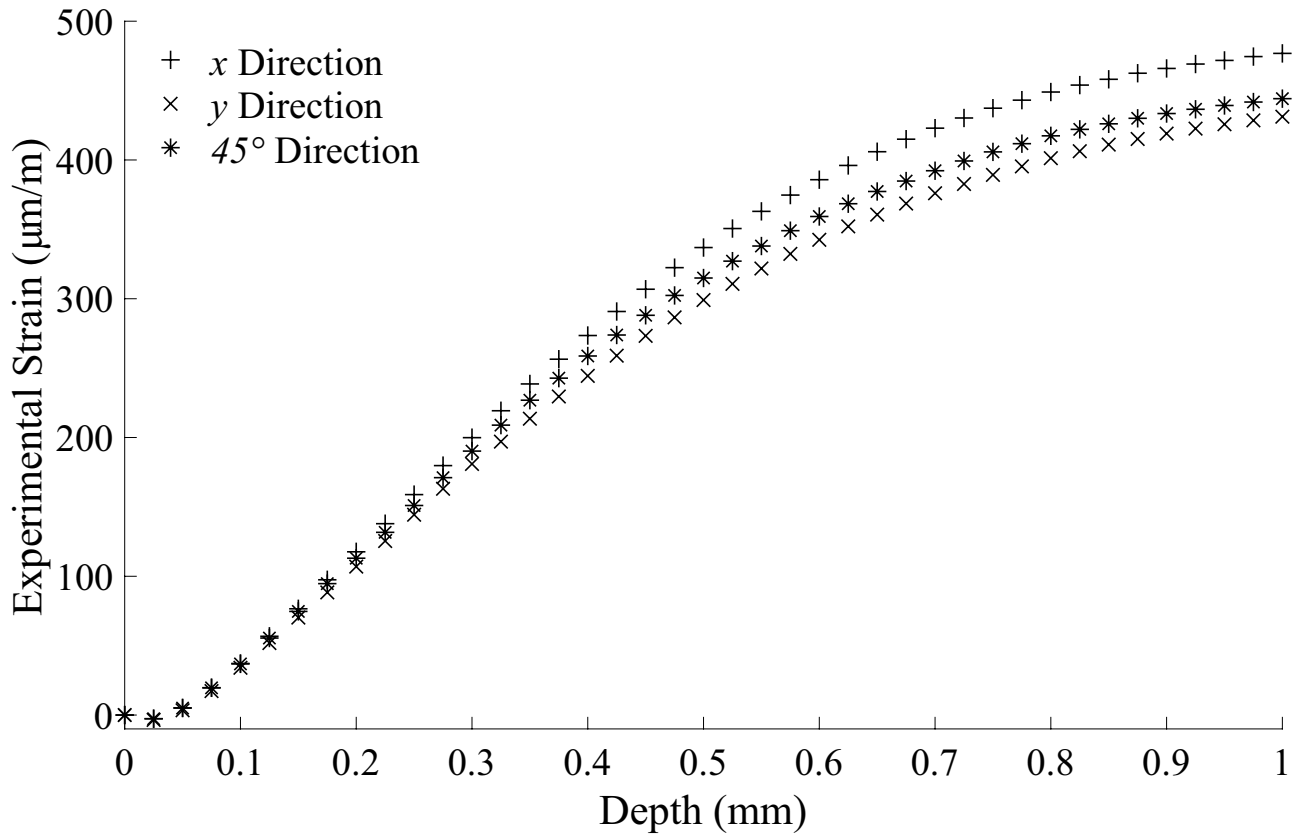


Fig. 1 Strain variation with depth in the x , y and 45° strain gauge directions

ble in this particular case. In general, however, it is possible in principle to obtain the necessary series expansion coefficients through numerical integration of the ASTM coefficients, provided that the plate thickness and hole diameters are within the guidelines specified by the ASTM standard. There was, however, no real benefit to be gained from integration of unit pulse coefficients in this particular case. The additional computation required to obtain the coefficients for series expansion was negligible since this merely required the inclusion of additional load cases within the FE model required to obtain the coefficients for the integral method. The calibration coefficients were calculated using MSC Nastran FE analysis. The specimen was modelled using 124 HEX8 type 3D elements through the thickness, 24 elements of $50\ \mu\text{m}$ height through the first 1.2 mm from the surface and 100 elements through the remaining thickness with linearly increasing element height towards the bottom of the plate. While the use of a 2D model would have offered benefits in terms of reduced run times and finer discretization of the r - z plane with a modest number of elements, the computational time requirement in this study was not a limitation. It was consequently elected to

use 3D modelling as was done by Alegre et al. [32] who found very good agreement with the ASTM coefficients for the case of thick samples with a coarser mesh than used in this work, and who found that results were practically unaffected by further mesh refinement. FE models with hole diameters between 1.70 mm and 1.90 mm, with 0.05 mm spacing increments, were used such that calibration matrices for any experimental hole diameter within this range can be found by interpolation. A quarter model was used with symmetric and anti-symmetric boundary conditions depending on the applied loading. Eigenstrain distributions for the series expansion method were applied to the FE model by means of through-thickness temperature variations defined by power series functions and dummy thermal expansion coefficients. Elements in the first 1.2 mm below the surface were assigned a coefficient of thermal expansion of unity in the x , y or in-plane shear direction and the remaining elements were assigned a coefficient of thermal expansion of zero.

Each applied eigenstrain distribution results in mechanical strain redistribution which generates a through-thickness stress distribution. For illustrative purposes, the stress dis-



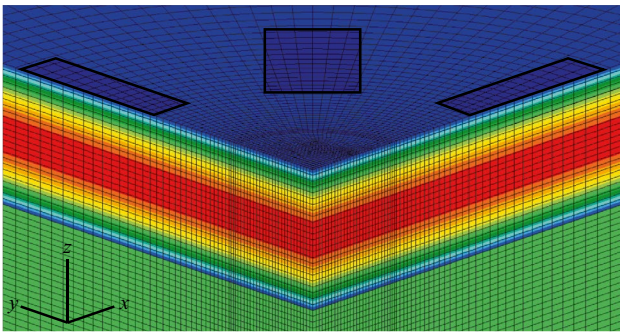


Fig. 2 σ_x distribution generated by 2nd order eigenstrain in the x direction, including the strain gauge grid locations

tribution in the x direction due to eigenstrain generated by a 2nd order temperature variation in the x direction is presented in Fig. 2. The mesh around the hole, on the top surface, and the position of the strain gauge grid locations (highlighted) are also presented. The displacements of all the nodes in the region of the strain gauge grid locations were determined for each loading condition and hole depth. The nodal displacement data was then used with surface spline interpolation to determine the displacements around the perimeter of each grid. This allows calculation

of the calibration coefficients from the longitudinal and transverse strains at each strain gauge location, including correction for the effect of transverse sensitivity [29]. IHD was simulated by incrementally removing layers of elements from the region of the hole.

A total of 47 depth increments of 25 μm , including zero depth, up to a maximum depth of 1.15 mm were used experimentally. The additional strain data points beyond 1 mm were used in the series expansion approach to somewhat constrain the series at depths approaching 1 mm and so reduce the stress uncertainty in this region. Additionally, Equation (5) of the series expansion approach requires that ϵ_{meas} and C follow the same depth distribution. Since the depth increment used in the computational work to determine C was twice that used experimentally, spline interpolation was used to double the number of coefficients in C since these coefficients vary smoothly with depth.

As the order of series expansion is increased, the least-squares fit to the experimental strain data is improved as can be seen in Fig. 3 for the x direction strain gauge, where a 4th order series expansion is not able to accurately fit the experimental strain data and a higher order series must be used. Although a 6th order series is able to fit the experimental strain data fairly accurately, this alone does

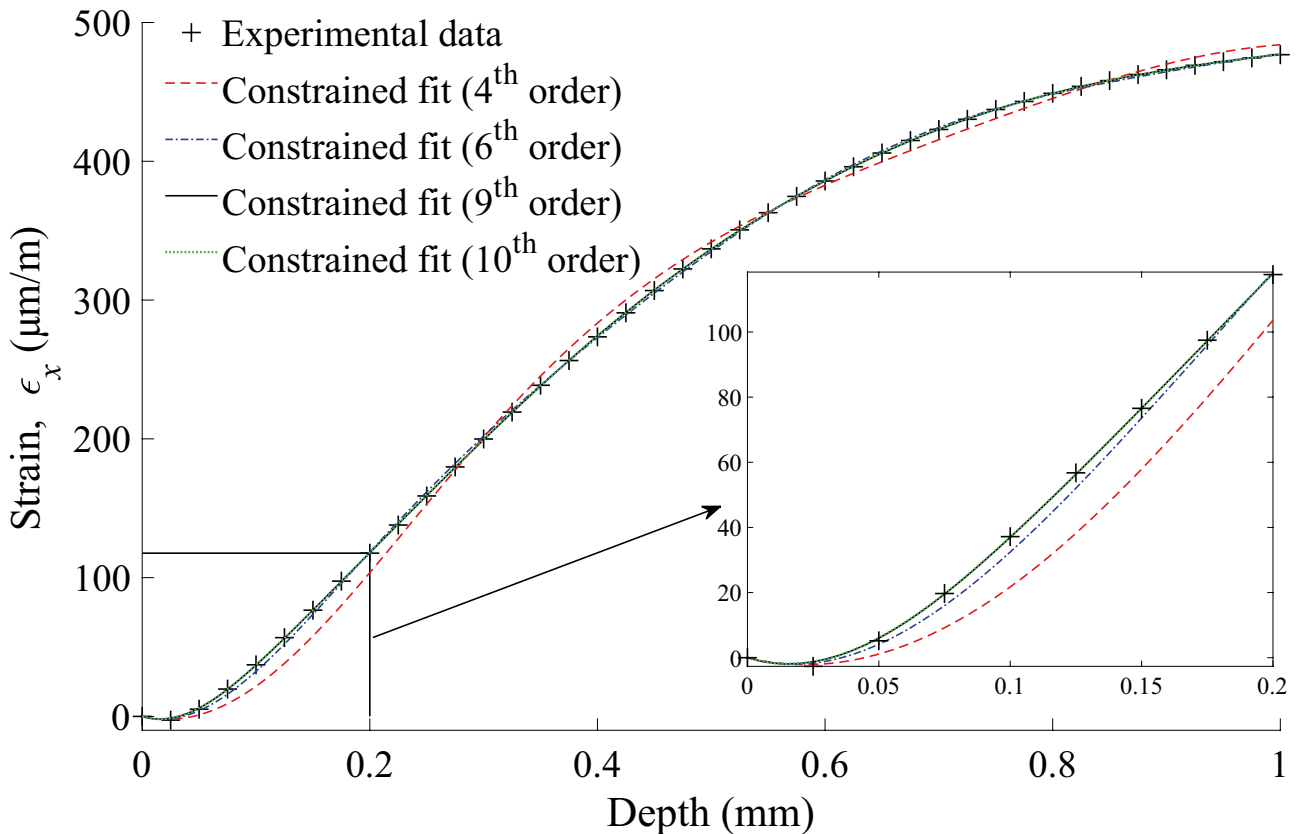


Fig. 3 Constrained least-squares fits to strain data in the x direction using 4th, 6th, 9th and 10th order series



not guarantee convergence to a stress solution and higher order series may be required. In this instance, both 9th and 10th order series are able to accurately fit the experimental strain data and can be said to have converged. Since higher order series can become unstable, however, it is crucial that a series order which can fully describe the actual residual stress distribution is found before instabilities become apparent. A robust uncertainty analysis of the residual stress distribution is, therefore, required so that convergence can be assured.

The FE model used for series expansion was also used to determine the calibration matrices for the integral method by using PLOAD4 cards to apply an equi-biaxial stress (for matrix \bar{a}) and a pure shear stress (for matrix \bar{b}) to the face of the hole for every loading increment at each incremental depth. For the integral method, every second experimental strain datum was used such that the 50 μm depth increments correspond with the calculated \bar{a} and \bar{b} matrices from the FE model.

Propagation of Uncertainties

Uncertainty in the calculated stress distributions was estimated through the use of Monte Carlo simulation as per JCGM 101:2008 [33]. Only the predominant experimental and computational uncertainty sources are considered in this work, provided in Table 3. Although other uncertainty sources such as the uncertainty in measured hole diameter [28] and hole offset [34], for example, can be easily incorporated, their effects on the stress uncertainty are negligible compared to the uncertainty sources considered here [28]. Ten thousand Monte Carlo trials were simulated for each order of the constrained and standard series expansion approaches and for the integral method.

XRD measurement uncertainty reported by the Proto software only includes the estimated uncertainty associated with statistical errors and the elliptical least-squares

fit of the $\sin^2 \psi$ plot. The larger than usual uncertainty is due to the adverse effects of large grain sizes in aluminium alloy 7075-T651, and the texture and high stress gradient near the surface due to the effects of the LSP process on the aluminium material [5].

Each IHD strain measurement was adjusted for the uncertainty in its respective depth increment, and all were adjusted for the uncertainty in zero depth. Spline interpolation was then used to determine the strains at the depth increments inherent to the C or \bar{a} and \bar{b} matrices and referenced to the zero depth of that trial. The misfit between the least-squares solution of each series order and the experimental strain data was included as an additional measurement uncertainty at each incremental depth. The misfit due to the use of Tikhonov regularization with the integral method was treated similarly. The C and S matrices were appropriately scaled according to independent variations in material properties within each Monte Carlo trial. Uncertainty in the material properties was included in the integral method within Equations (2)–(4).

The strain vector (ϵ_{meas}), calibration matrix (C), stress matrix (S) and XRD measurements of each Monte Carlo trial were used with Equations (13), (11) and (6) for the constrained series method and Equations (5) and (6) for standard series expansion to determine the stress distribution for that trial. The calibration matrices (\bar{a} and \bar{b}) of each Monte Carlo trial were used with Equations (2)–(4) in the case of the integral method. The stress uncertainty at a particular depth was determined for each method by evaluating the standard deviation in the calculated stress at that depth from the ten thousand Monte Carlo trials.

Selection of Series Order

A practical challenge when using series expansion is the discontinuous nature of the stress results as the series order is increased. At lower orders, large changes occur between

Table 3 Uncertainty sources and their assigned probability density functions

x_i	Description	$p(x_i)$	Type	Nominal value, uncertainty
σ_{xXRD}	Stress in the x direction from XRD measurements	Normal	B	60.4 MPa, 33.5 MPa
σ_{yXRD}	Stress in the y direction from XRD measurements	Normal	B	70.4 MPa, 15.4 MPa
τ_{xyXRD}	Shear stress from XRD measurements	Normal	B	-58.5 MPa, 38.7 MPa
E	Young's Modulus	Normal	B	71700 MPa, 3%
ν_{12}	Poisson's ratio	Normal	B	0.33, 3%
z_k	Incremental depths	Rectangular	B	25 μm , 0.5 μm
z_0	Zero depth	Rectangular	B	0 μm , 10 μm
ϵ_m	Indicated experimental strain	Normal	B	Figure 1, 1.6%
ϵ_{noise}	Experimental noise	Normal	A	Figure 1, 1 $\mu\text{m}/\text{m}$
FE	Finite element calculations	Normal	B	0, 2%



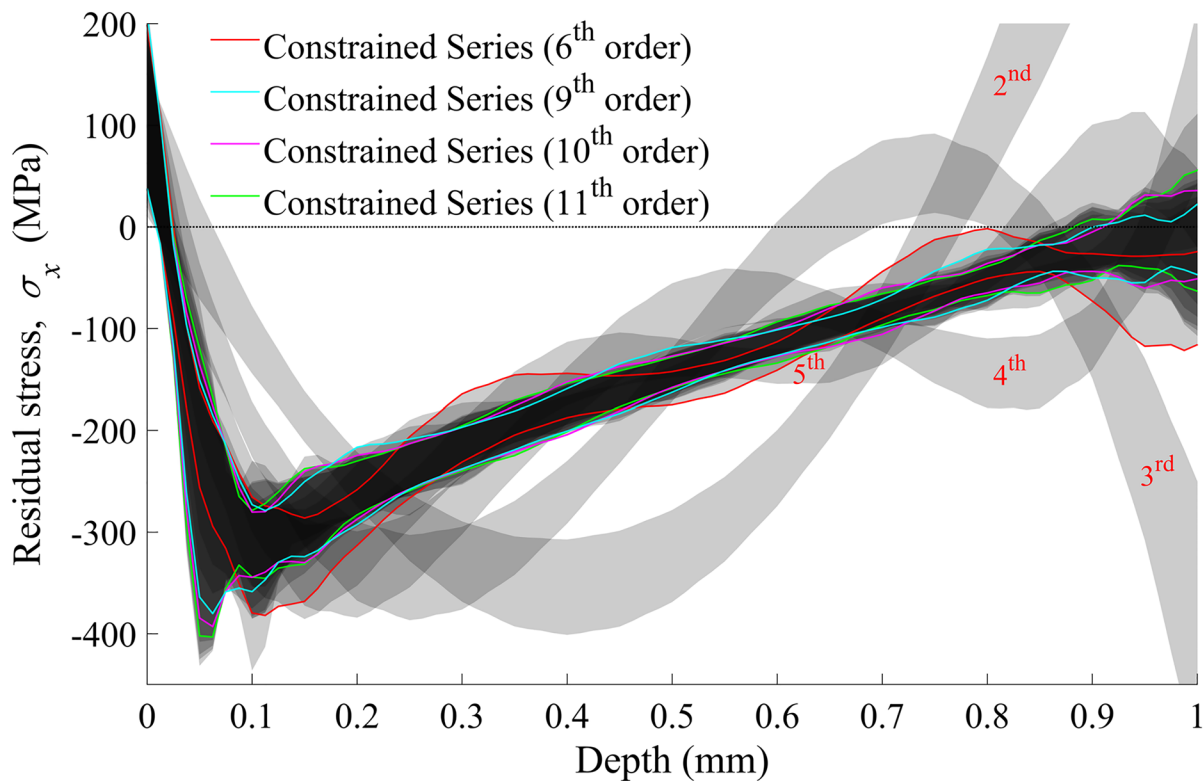


Fig. 4 Overlap of the uncertainty bounds in σ_x for 2nd to 15th order series

each stress distribution in the sequence. In general, however, low order series expansion should not be used. Instead, series expansion of high enough orders should be used such that the variation in stress distributions from order to order becomes negligible as the series converge. The issue of convergence therefore becomes a paramount consideration. The series order that best approximates the residual stress distribution for the experimental strain data was determined as the series order with the lowest RMS uncertainty, from those series orders that have converged [29]. The calculated stress distribution and associated uncertainty in the x direction for orders 2 to 15 of the constrained series method are shown in Fig. 4. The uncertainties in all figures correspond to ± 2 standard deviations. The uncertainty bounds in the y direction for orders 2 to 15 are similar to those in the x direction and the corresponding figure is therefore omitted in the interest of brevity. All stress uncertainty bounds in Fig. 4 are plotted using light grey such that convergence of a number of orders gives rise to darker areas. The remaining light grey areas correspond to low order series, 2nd to 5th order, which are unable to describe the actual stress distribution, and to higher order series where the uncertainty bounds start to diverge due to increasing instability. It is clear in Fig. 4 that as the series order increases from 2 to 5, the series

converge towards the actual residual stress distribution. The 6th order series has the lowest total uncertainty, but it has not converged and can therefore not be selected, similarly for the 7th and 8th order series. The orders 9 to 11 have converged and the 9th order series is selected as the best solution for this experimental data set as it has the lowest total RMS stress uncertainty of the series orders that have converged. Interestingly, the best series order for use in the standard series expansion method is one lower than that in the constrained solution. This difference arises because the imposition of constraints removes a degree of freedom from the solution in each stress direction and so an additional term is required in the constrained solution to get the same descriptive capability.

Results and Discussion

The least-squares fits of the constrained 9th order series to the experimental strain data are shown in Fig. 5 with associated uncertainties. The strain uncertainty due to the inability of the constrained 9th order series to exactly match the measured strain data is included in this figure. The calculated stress distributions and associated uncertainties of



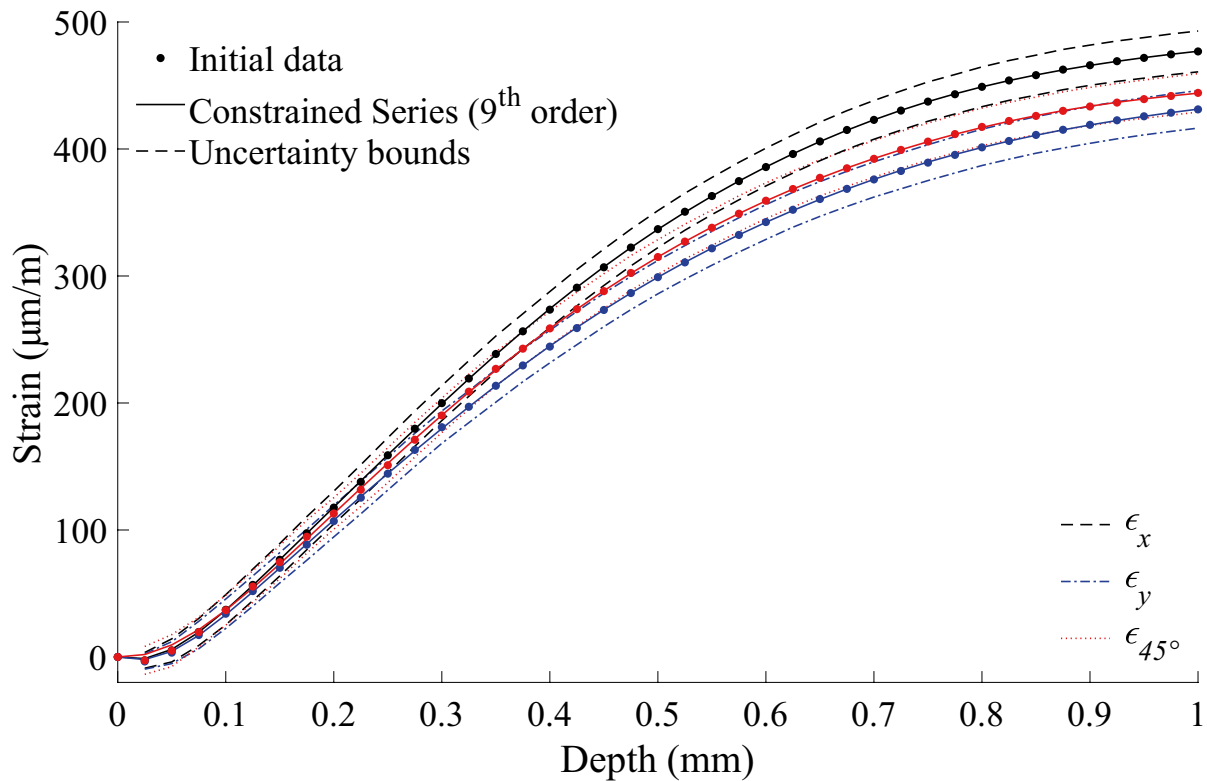


Fig. 5 Least-squares fits to the experimental strain data using the constrained 9th order series

the constrained 9th order series are shown in Fig. 6. The solid line corresponds to the the mean value of the calculated residual stress for all Monte Carlo simulations at each depth increment and the dashed lines are the upper and lower uncertainty bounds which correspond to ± 2 standard deviations of the Monte Carlo simulations. As expected, the LSP-induced residual stress distributions in the x and y directions are similar and the shear stress is close to zero. It is clear that a large tensile stress exists near the surface and that the combination of LSP parameters used in this particular study did not result in the desired compressive stress on the surface. Plasticity effects were not included since the maximum mean compressive stress is only 63% of the material yield strength. The FE model shown in Fig. 2 revealed that the maximum von Mises stress during material removal was 505.5 MPa on the flat base of the hole when the hole depth was 0.25 mm. This stress, although some 0.4% above yield, will not have any meaningful impact on the results and, in fact, some small unmodelled hole-bottom fillet radius would have existed at this corner of the hole, reducing this stress concentration somewhat in practice.

The calculated stress distributions and associated uncertainties of the standard series expansion and regularized

integral methods are shown with those obtained using the constrained series method in Figs. 7 and 8. The magnitude and form of the residual stress distributions and uncertainties compare favourably. Standard series expansion defines the residual stress distribution well but exhibits high uncertainty in stress near the surface since curve fitting methods tend to give their least reliable results at their ends. It is evident from Figs. 7 and 8 that standard series expansion does not offer any significant benefit over the integral method for near-surface stress measurement. It is clear that at the first stress datum of the integral method, the stress result and accompanying uncertainty of the standard series expansion and integral methods are the same. There is therefore no comparative advantage between the two methods on this front. In the case of the constrained series, the instability near the surface is reduced but at the expense of greater instability elsewhere, in particular the region of maximum compressive stress. The constrained series method significantly reduces the uncertainty in stress at the surface from 109.1 ± 73.4 MPa to 123.8 ± 43.0 MPa in the x direction and 118.3 ± 72.4 MPa to 133.0 ± 20.8 MPa in the y direction. Imposition of constraints on the regularized integral method should also be possible and would



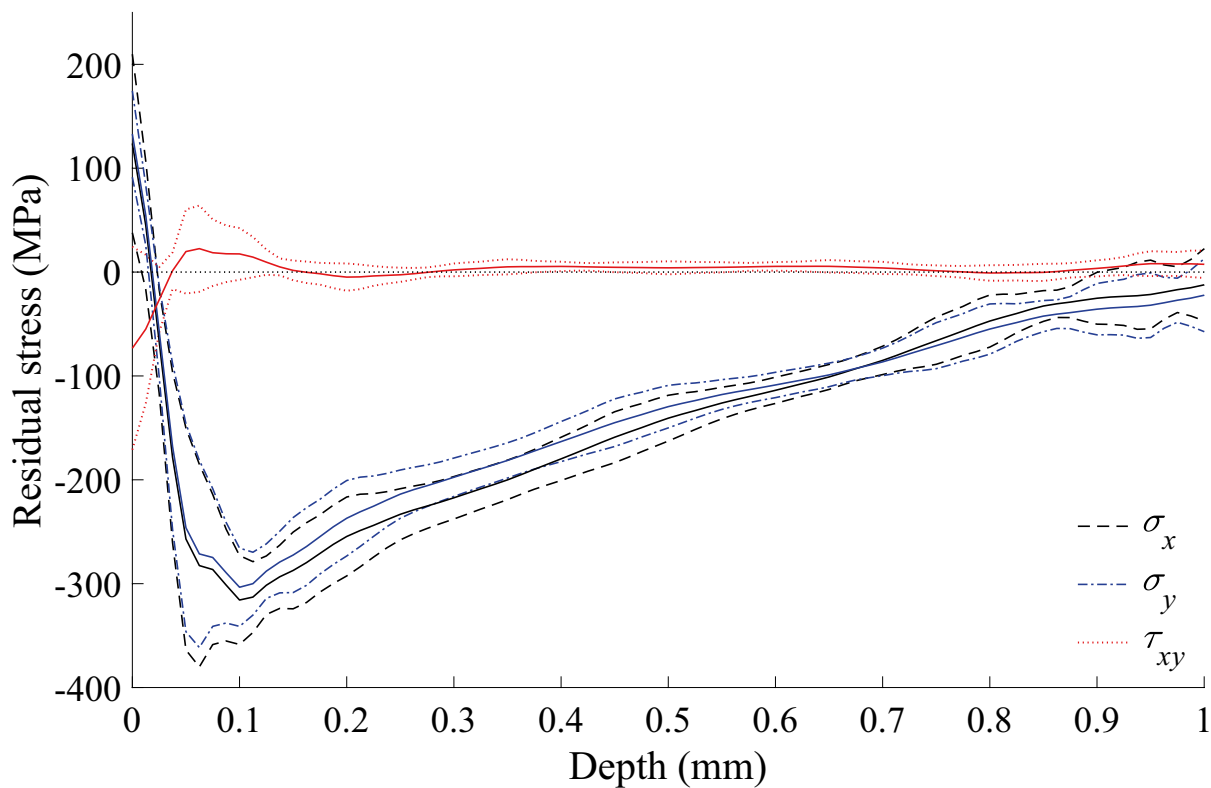


Fig. 6 Stress distributions and associated uncertainties obtained using the constrained 9th order series

presumably yield similar results to those obtained using constrained series expansion. Additionally, the continuity condition of the regularized solution and the small depth between the surface and the XRD data should enable a good estimation of the surface stress, similar to series expansion, and again it is expected that these answers would be similar. Table 4 shows the RMS uncertainty in stress over 1 mm for each computational method arising from each uncertainty source as well as the combined uncertainty, $u(Z)$.

Table 4 shows that zero depth position and noise in the experimental strains are some of the largest sources of uncertainty in stress. The series expansion methods are more tolerant of noise in the strain data due to least-squares curve fitting. Interestingly, the constrained series is less effected by noise in the experimental strains and zero depth position since it achieves a more stable fit to the strain data near the surface. However, the XRD measurements that help constrain the series near the surface introduce an additional stress uncertainty over the 1 mm depth which increases the total uncertainty of the constrained series to slightly above that of the unconstrained series. With more accurate XRD

results in less textured material such as steel, this additional uncertainty is reduced and the overall uncertainty for the constrained series is lower than that of the standard series expansion approach. For illustrative purposes, Table 5 presents the breakdown of RMS stress uncertainty through the 1 mm depth and the respective surface stresses with their accompanying uncertainties resulting from varying only the uncertainty in XRD results of Table 3 across a broad range of magnitudes which include the typical value of ± 20 MPa [9, 12]. As expected, the total uncertainty decreases with improved XRD accuracy until, at an XRD uncertainty of about ± 20 MPa, the constrained series method outperforms standard series expansion. The uncertainty in surface stress also reduces with improved XRD accuracy, but cannot be eliminated entirely because of the inherent uncertainty in IHD results. As can be seen in Fig. 9, the effect of XRD uncertainty on the stress distribution is localised to the near-surface measurements. The IHD uncertainty dominates as the hole depth increases so that the XRD uncertainty has little to no effect on the stress uncertainty below a depth of about 0.1 mm.



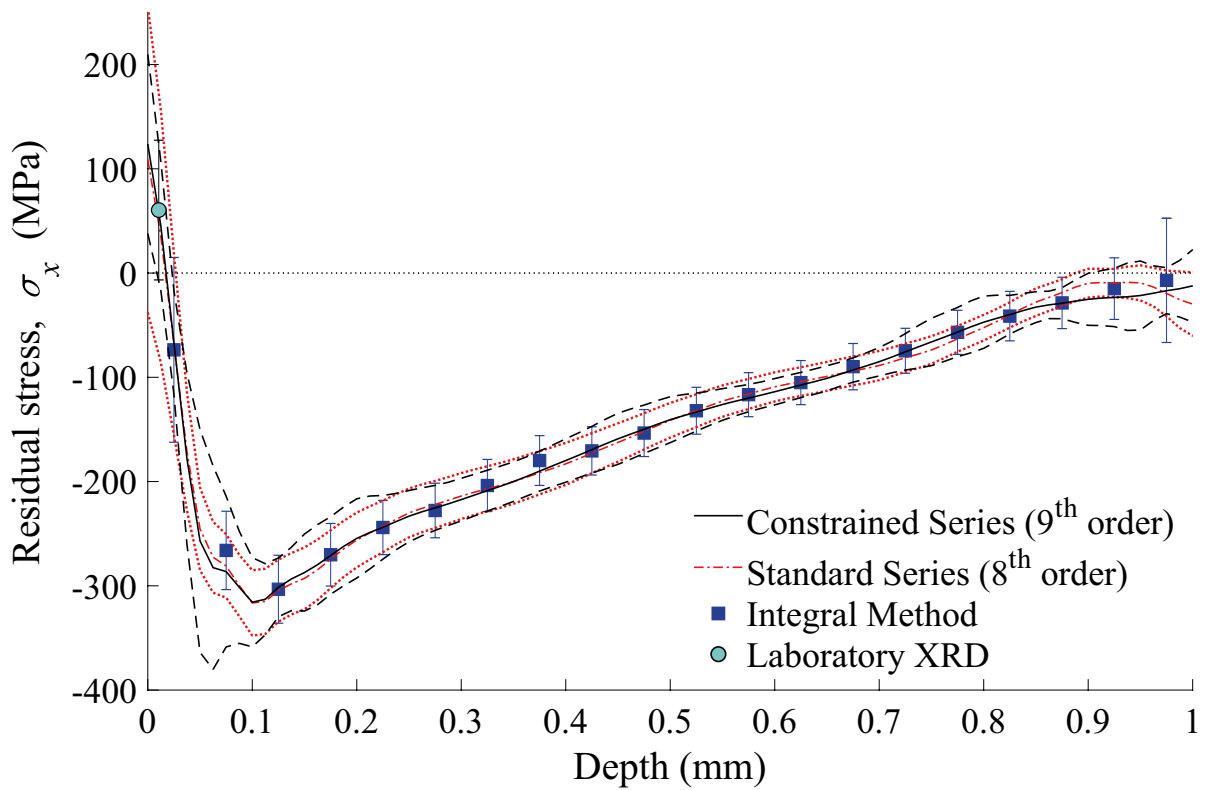


Fig. 7 σ_x distributions and associated uncertainties of each method

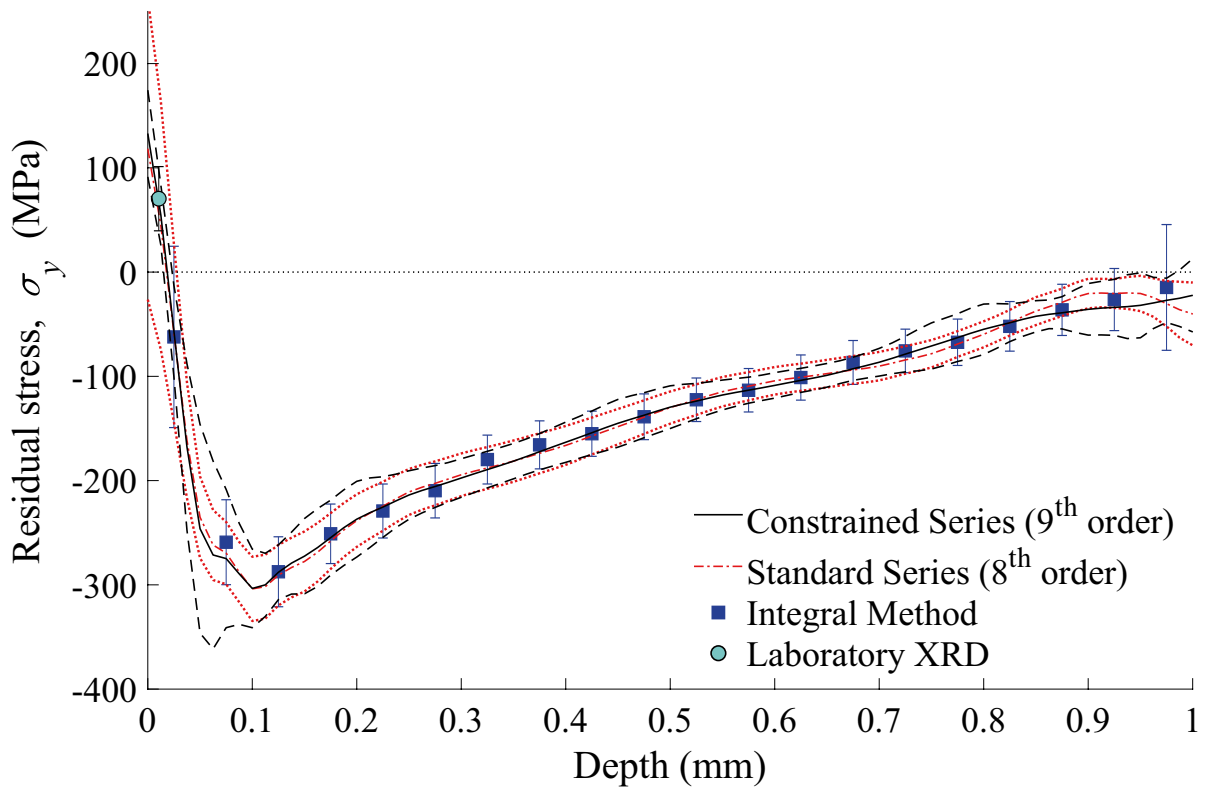


Fig. 8 σ_y distributions and associated uncertainties of each method



Table 4 Breakdown of RMS uncertainty in stress arising from each uncertainty source, x_i

x_i	Contribution to $u(\sigma_x)$ [MPa]			Contribution to $u(\sigma_y)$ [MPa]			Contribution to $u(\tau_{xy})$ [MPa]		
	Constrained Series	Series Expansion	Integral Method	Constrained Series	Series Expansion	Integral Method	Constrained Series	Series Expansion	Integral Method
<i>XRD</i>	7.423	-	-	3.656	-	-	8.338	-	-
<i>E</i>	4.996	5.084	4.962	4.682	4.800	4.656	0.118	0.128	0.108
ν_{12}	1.499	1.539	1.194	1.522	1.551	1.194	0.065	0.054	0.000
z_k	0.652	0.734	1.338	0.630	0.704	1.314	0.050	0.051	0.001
z_0	11.827	12.240	10.214	11.551	11.936	9.892	0.458	0.568	0.278
ϵ_m	2.668	2.716	2.650	2.501	2.558	2.487	0.062	0.062	0.057
ϵ_{noise}	4.781	5.265	11.141	4.775	5.256	11.174	2.853	3.700	3.728
<i>FE</i>	4.703	4.788	3.261	4.409	4.509	3.058	0.110	0.109	0.072
<i>Misfit</i>	1.153	2.374	3.543	1.384	2.744	4.420	1.575	2.237	2.464
$u(Z)$	16.698	15.625	17.044	14.972	15.249	16.939	8.965	4.392	4.157

Table 5 Breakdown of RMS uncertainty in stress resulting from reducing only the uncertainty in XRD results

	Total uncertainties [MPa]			Surface stresses [MPa]		
	σ_x	σ_y	τ_{xy}	σ_x	σ_y	τ_{xy}
Series Expansion	15.625	15.249	4.392	109.1±73.4	118.3±72.4	-10.3±22.2
Constrained Series, $u(XRD) = 40$ MPa	17.452	17.078	9.194	124.1±51.7	133.4±51.8	-72.4±50.3
Constrained Series, $u(XRD) = 30$ MPa	16.231	15.928	7.218	123.1±38.0	133.5±38.5	-72.7±37.5
Constrained Series, $u(XRD) = 20$ MPa	15.553	15.153	5.488	123.5±26.3	133.5±26.6	-73.2±25.6
Constrained Series, $u(XRD) = 10$ MPa	15.142	14.704	3.941	123.3±14.8	133.3±14.6	-73.0±12.7
Constrained Series, $u(XRD) = 0$ MPa	14.950	14.541	3.315	123.4±7.5	133.2±7.3	-73.0±1.2

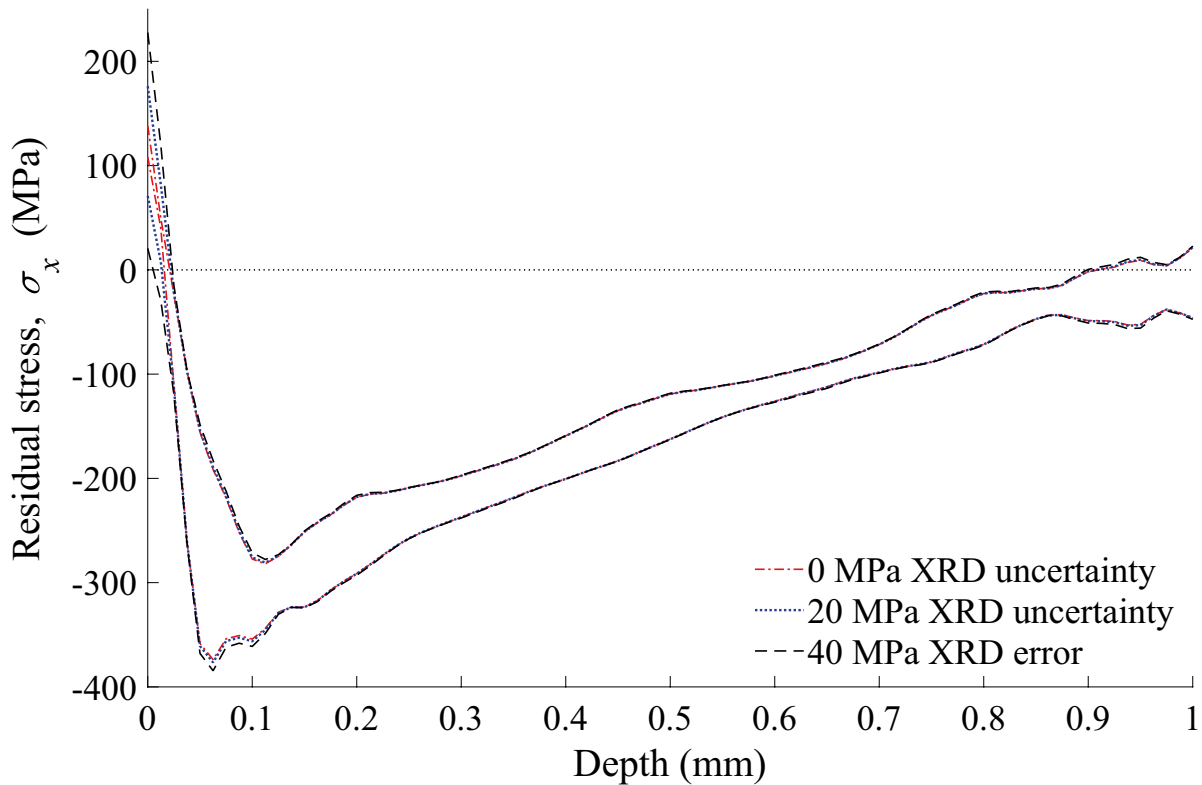


Fig. 9 σ_x uncertainty distributions for varying magnitudes of XRD uncertainty



Conclusions

The IHD method is prone to high uncertainty in near-surface residual stress measurements, irrespective of the computational method employed. A hybrid method has been developed that makes use of near-surface XRD measurements to constrain the least-squares solution of IHD series expansion and thereby reduce the stress uncertainty near the surface. This allows the complete stress distribution up to 1 mm depth to be fully defined with increased accuracy using IHD. A comprehensive demonstration of this computational method for IHD has been performed on an aluminium alloy 7075 plate of 10 mm thickness that underwent LSP treatment. The use of constrained series expansion was compared to the widely used regularized integral method, and standard series expansion. While there is a strong correlation in the calculated stress distributions of all three computational methods, the constrained series expansion method significantly reduces the uncertainty in residual stress in the near-surface region because of its incorporation of XRD data from this region. It is believed that integral method computations would be stabilised similarly if XRD surface stress data were used to impose constraints on the regularized solution.

Acknowledgements The authors wish to thank Dr Daniel Glaser of the National Laser Centre (NLC) at the Council for Scientific and Industrial Research (CSIR), Pretoria, South Africa, for conducting the XRD measurements used in this work. The authors wish to thank the Rental Pool Programme from the National Laser Centre (NLC) at the Council for Scientific and Industrial Research (CSIR), Pretoria, South Africa.

Declarations

Conflicts of interest The authors declare that they have no conflict of interest.

References

- Ding K, Ye L (2006) Laser shock peening Performance and process simulation. Woodhead Publishing in materials. Taylor & Francis
- Hammond DW, Meguid SA (1990) Crack propagation in the presence of shot-peening residual stresses. *Eng Frac Mech*, 37(2):373–387 [https://doi.org/10.1016/0013-7944\(90\)90048-L](https://doi.org/10.1016/0013-7944(90)90048-L)
- Kandil F, Lord D, Fry A (2001) A review of residual stress measurement methods: A guide to technique selection, National Physical Laboratory Materials Centre: Teddington, UK, Technical report
- Cullity BD, Stock SR (2001) Elements of X-ray Diffraction, Third Edition. Prentice-Hall
- Fitzpatrick ME, Fry AT, Hholloway P, Kandil FA, Shackleton J, Suominen L (2005) Determination of residual stresses by x-ray diffraction. ISSN: 1368-6550
- Macherauch E, Müller P (1961) Das sin²y-verfahren der röntgenographischen spannungsmessung. *Zeitschrift für Angewandte Physik*, 13:305–312
- Valentini E, Beghini M, Bertini L, Santus C, Benedetti M (2011) Procedure to perform a validated incremental hole drilling measurement: Application to shot peening residual stresses. *Strain*, 47(s1):e605–e618 <https://doi.org/10.1111/j.1475-1305.2009.00664.x>
- Li A, Ji V, Lebrun JL, Ingelber G (1995) Surface roughness effects on stress determination by the X-ray diffraction method. *Exp Tech*, 19(2):9–11 <https://doi.org/10.1111/j.1747-1567.1995.tb00840.x>
- Withers PJ, Bhadeshia HKDH (2001) Residual stress. Part 1: Measurement techniques. *Mat Sci Tech*, 17(4):355–365 <https://doi.org/10.1179/026708301101509980>
- Fry AT, Kandil FA (2002) A study of parameters affecting the quality of residual stress measurements using XRD. In *Residual Stresses VI, ECRS6*, Volume 404 of Materials Science Forum, pages 579–586. Trans Tech Publications Ltd <https://doi.org/10.4028/www.scientific.net/MSF.404-407.579>
- François M, Convert F, Branchu S (2000) French round-robin test of X-ray stress determination on a shot-peened steel. *Exp Mech*, 40(4):361–368 <https://doi.org/10.1007/BF02326481>
- SAE International (2003) Residual Stress Measurement by X-ray Diffraction: HS-784. HS (Society of Automotive Engineers). SAE International
- ASTME837-13a (2013) Standard test method for determining residual stresses by the hole-drilling strain-gage method. ASTM International, West Conshohocken, PA <https://astm.org>
- Schajer GS (1981) Application of Finite Element Calculations to Residual Stress Measurements. *J Eng Mat Tech*, 103(2):157 <https://doi.org/10.1115/1.3224988>
- Schajer GS (1988) Measurement of non-uniform residual stresses using the hole-drilling method. Part II. Practical application of the integral method. *J Eng Mat Tech*, Transactions of the ASME, 110(4):344–349 <https://doi.org/10.1115/1.3226059>
- Tikhonov AN, Goncharky AV, Stepanov VV, Yagola AG (1995) Numerical Methods for the Solution of Ill-Posed Problems. Kluwer, Dordrecht
- Blödorn R, Bonomo LA, Viotti MR, Schroeter RB, Albertazzi A (2017) Calibration Coefficients Determination Through Fem Simulations for the Hole-Drilling Method Considering the Real Hole Geometry. *Exp Tech* <https://doi.org/10.1007/s40799-016-0152-3>
- Peral D, Correa C, Diaz M, Porro JA, de Vicente J, Ocaña JL (2017) Measured strains correction for eccentric holes in the determination of non-uniform residual stresses by the hole drilling strain gauge method. *Materials and Design* <https://doi.org/10.1016/j.matdes.2017.06.051>
- Beghini M, Bertini L, and Mori LF (2010) Evaluating non-uniform residual stress by the hole-drilling method with concentric and eccentric holes. Part II: Application of the influence functions to the inverse problem. *Strain*, 46(4):337–346 <https://doi.org/10.1111/j.1475-1305.2009.00684.x>
- Barsanti M, Beghini M, Bertini L, Monelli B, Santus C (2016) First-order correction to counter the effect of eccentricity on the hole-drilling integral method with strain-gage rosettes. *J Strain Anal Eng Design* <https://doi.org/10.1177/0309324716649529>
- Nobre JP, Kornmeier M, Scholtes B (2018) Plasticity Effects in the Hole-Drilling Residual Stress Measurement in Peened Surfaces. *Exp Mech* <https://doi.org/10.1007/s11340-017-0352-5>
- Beghini M, Bertini L, Santus C (2010) A procedure for evaluating high residual stresses using the blind hole drilling method, including the effect of plasticity. *J Strain Anal Eng Design*, 45(4):301–318 <https://doi.org/10.1243/03093247JSA5>
- Vishay Precision Group (2010) Measurement of Residual Stresses by the Hole-Drilling Strain Gage Method, Tech Note TN-503. Technical report
- Nobre JP, Kornmeier M, Dias AM, Scholtes B (2000) Use of the hole-drilling method for measuring residual stresses in highly



- stressed shot-peened surfaces. *Exp Mech*, 40:289–297 <https://doi.org/10.1007/BF02327502>.
25. Valentini E, Santus C, Bandini M (2011) Residual stress analysis of shot-peened aluminum alloy by fine increment hole-drilling and x-ray diffraction methods. *Procedia Engineering*, 10:3582 – 3587, 2011. 11th International Conference on the Mechanical Behavior of Materials (ICM11) <https://doi.org/10.1016/j.proeng.2011.04.589>
 26. Nobre JP, Polese C, and van Staden SN (2020) Incremental hole drilling residual stress measurement in thin aluminum alloy plates subjected to laser shock peening. *Exp Mech*, 60(1):553–564 <https://doi.org/10.1007/s11340-020-00586-5>.
 27. Prime MB, Hill MR (2006) Uncertainty, Model Error, and Order Selection for Series-Expanded, Residual-Stress Inverse Solutions. *J Eng Mat Tech*, 128(2):175 <https://doi.org/10.1115/1.2172278>
 28. Smit TC, Reid RG (2020) Use of Power Series Expansion for Residual Stress Determination by the Incremental Hole-Drilling Technique. *Exp Mech*, 60(9):1301–1314 <https://doi.org/10.1007/s11340-020-00642-0>.
 29. Smit TC, Reid RG (2018) Residual Stress Measurement in Composite Laminates Using Incremental Hole-Drilling with Power Series. *Exp Mech*, 58(8):1221–1235 <https://doi.org/10.1007/s11340-018-0403-6>.
 30. ASM International (1990) *ASM Handbook Volume 2: Properties and Selection: Nonferrous Alloys and Special-Purpose Materials*.
 31. Noyan IC, Cohen JB (1987) *Residual Stress: Measurement by Diffraction and Interpretation*. Springer-Verlag New York <https://doi.org/10.1007/978-1-4613-9570-6>.
 32. Alegre JM, Diaz A, Cuesta II, and Mansi JM (2019) Analysis of the Influence of the Thickness and the Hole Radius on the Calibration Coefficients in the Hole-Drilling Method for the Determination of Non-uniform Residual Stresses. *Exp Mech*, 59(1):79–94 <https://doi.org/10.1007/s11340-018-0433-0>
 33. BIPM, IEC, IFCC, ILAC, IUPAC, IUPAP, ISO, and OIML. Evaluation of measurement data Supplement 1 to the Guide to the expression of uncertainty in measurement Propagation of distributions using a Monte Carlo method, JCGM 101: 2008. 2008
 34. Smit TC, Reid RG (2020) Tikhonov regularization with Incremental Hole-Drilling and the Integral Method in Cross-Ply Composite Laminates. *Exp Mech*, 60(8):1135–1148 <https://doi.org/10.1007/s11340-020-00629-x>.

Publisher's Note Springer Nature remains neutral with regard to jurisdictional claims in published maps and institutional affiliations.

